VIP Artificial Photosynthesis Very Important Paper

International Edition: DOI: 10.1002/anie.202000929
German Edition: DOI: 10.1002/ange.202000929

Semiconductor/Covalent-Organic-Framework Z-Scheme Heterojunctions for Artificial Photosynthesis

*Mi Zhang[+], Meng Lu[+], Zhong-Ling Lang[+], Jiang Liu, Ming Liu, Jia-Nan Chang, Le-Yan Li, Lin-Jie Shang, Min Wang, Shun-Li Li, and Ya-Qian Lan**

Abstract: *A strategy to covalently connect crystalline covalent organic frameworks (COFs) with semiconductors to create stable organic–inorganic Z-scheme heterojunctions for artificial photosynthesis is presented. A series of COF–semiconductor Z-scheme photocatalysts combining water-oxidation semiconductors (TiO_2, Bi_2WO_6, and α-Fe_2O_3) with CO_2 reduction COFs (COF-316/318) was synthesized and exhibited high photocatalytic CO_2-to-CO conversion efficiencies (up to 69.67 $\mu mol\,g^{-1}\,h^{-1}$), with H_2O as the electron donor in the gas–solid CO_2 reduction, without additional photosensitizers and sacrificial agents. This is the first report of covalently bonded COF/inorganic-semiconductor systems utilizing the Z-scheme applied for artificial photosynthesis. Experiments and calculations confirmed efficient semiconductor-to-COF electron transfer by covalent coupling, resulting in electron accumulation in the cyano/pyridine moieties of the COF for CO_2 reduction and holes in the semiconductor for H_2O oxidation, thus mimicking natural photosynthesis.*

Introduction

Excessive emission of carbon dioxide (CO_2) produced from the burning of fossil fuels has caused energy and environmental issues that need to be resolved.[1] Inspired by natural photosynthesis, converting CO_2 and H_2O into carbohydrates and O_2 by solar energy is regarded as an ideal and green approach to solve this problem.[2] However, it is still challenging to integrate the CO_2 reduction reaction (CO_2RR) and H_2O oxidation reaction into one photosynthetic system and to couple them effectively.[2,3] Traditional Z-scheme heterojunctions assembled from two inorganic semiconductors into a single component with two separate functional sites has been considered as an approach that satisfies the aforementioned criteria.[3a] This type of Z-scheme system has been widely used in water splitting, while only a few studies have been conducted in the field of the CO_2RR because many vital aspects are difficult to solve simultaneously in most all-inorganic Z-scheme system: i) efficient light absorption; ii) fast CO_2 adsorption and diffusion; iii) suitable redox sites and band structure for simultaneous CO_2 reduction and H_2O oxidation; iv) fast separation and migration of photo-generated electrons and holes to the adsorbed CO_2 and H_2O molecules, respectively, at the active sites.[4] As a result, the photocatalytic efficiency of the CO_2 reduction for all-inorganic Z-scheme systems is still difficult to improve presently. The combination of functionalized organic components and inorganic semiconductors is an effective way to improve these factors, but the connectivity between them suffers from instability and the ineffectiveness of physical adsorption or the stacking force.[4a,5] On the contrary, employing catalysts with well-defined structures to further systematically study the reaction mechanisms is of great significance.[6]

Crystalline covalent organic frameworks (COFs), which have large surface areas and a tunable structure, are expected to provide an ideal scaffold for CO_2 adsorption, diffusion, and activation.[7] With suitable building blocks and functional organic groups, COFs have been shown to have a high visible-light absorption capacity and fast charge-carrier mobility.[8] Furthermore, many COF-based photocatalysts have been successfully used for the light-driven reduction of CO_2.[6a,7c–e] Meanwhile, many inorganic semiconductors (SCs, such as TiO_2, Bi_2WO_6, or α-Fe_2O_3) have been demonstrated to be outstanding photocatalysts that can achieve efficient H_2O photooxidation.[9] On this basis, functionally combining the water-oxidizing inorganic semiconductor with CO_2 reduction COFs to form heterogeneous Z-scheme systems may be a feasible strategy to enhance the efficiency of artificial photosynthesis, that is, simultaneously reduce CO_2 and oxidize water. The key to achieve this integration is whether the charge carrier can be effectively transferred between the semiconductor and the COF. Connection via covalent bonds is a good choice to address these problems, as it also provides a high stability for the photocatalyst.[10] However, no practical method for the effective covalent connection of organic porous materials and inorganic semiconductors is known yet.

In this work, we present a method for the fabrication of stable covalently linked organic–inorganic Z-scheme systems comprising COFs and inorganic oxide semiconductors for artificial photosynthesis (CO_2RR with H_2O). Polyarylether-(PAE)-COFs are a class of COFs that are condensed through

[*] M. Zhang,[+] M. Lu,[+] Dr. J. Liu, M. Liu, J.-N. Chang, L.-Y. Li, L.-J. Shang, M. Wang, Prof. S.-L. Li, Prof. Y.-Q. Lan
Jiangsu Collaborative Innovation Centre of Biomedical Functional Materials, School of Chemistry and Materials Science
Nanjing Normal University
No. 1, Wenyuan Road, Nanjing, 210023 (China)
E-mail: yqlan@njnu.edu.cn
Dr. Z.-L. Lang[+]
Key Laboratory of Polyoxometalate Science of the Ministry of Education, Faculty of Chemistry, Northeast Normal University
Changchun, 130000 (P. R. China)
[+] These authors contributed equally to this work.
Supporting information and the ORCID identification number(s) for the author(s) of this article can be found under: https://doi.org/10.1002/anie.202000929.

aromatic nucleophilic substitution between various *o*-difluorobenzene and catechol building blocks.[11] We chose 2,3,6,7,10,11-hexahydroxytriphenylene (HHTP) and tetrafluorophthalonitrile (TFPN) or 2,3,5,6-tetrafluoro-4-pyridinecarbonitrile (TFPC) as precursors to obtain two PAE-COFs, named COF-316 and COF-318, respectively. The strong electron-withdrawing substituents on the TFPN and TFPC building blocks make TFPN/TFPC prone to nucleophilic attacks by hydroxyl functionalities.[12] It is well known that various semiconductors can be functionalized by organic functional groups through covalent linking, especially oxide-semiconductors, which always contain hydroxyl functional groups on the surface.[13] Through this feature, semiconductors can be covalently connected to PAE-COFs. As a proof of concept, a series of COF/oxide-semiconductor heterojunctions (COF-SC: COF-TiO_2, Bi_2WO_6, and α-Fe_2O_3) were designed and synthesized for photosynthetic gas–solid CO_2 reduction using H_2O as the electron donor, without the help of additional photosensitizers and sacrificial agents. As expected, the covalently linked COF-318-TiO_2 Z-scheme catalyst showed the highest CO production rate of 69.67 $\mu mol\,g^{-1}\,h^{-1}$, 5.2 times higher than the pure COF-318 (13.3 $\mu mol\,g^{-1}\,h^{-1}$) and six times higher than TiO_2 (11.8 $\mu mol\,g^{-1}\,h^{-1}$), also much higher than the plain physical mixture (29.3 $\mu mol\,g^{-1}\,h^{-1}$), which is one of the best performances of all the reported catalysts for overall CO_2 reduction with H_2O to our knowledge. Moreover, COF-318-TiO_2, in which pyridine and cyano moieties coexist, has a higher performance than COF-316-TiO_2 (57.16 $\mu mol\,g^{-1}\,h^{-1}$), which only contains cyano groups. From experiment and density functional theory (DFT) calculations, we illustrate the electron-transfer direction and CO_2-reduction mechanisms. The photogenerated electrons driven by photo-irradiation transfer effectively from the semiconductor to the COF by covalent coupling, resulting in the electrons accumulating at the cyano/pyridine active sites of the COF for the CO_2RR, while positively charged holes in semiconductor enable H_2O oxidation, thus mimicking natural photosynthesis. From mechanism analysis, the coexistence of pyridine and cyano groups reduces the overall energy barrier for the reduction of CO_2. Our results provide a versatile route for the future construction of COF–semiconductor heterojunctions and new possibilities for the development of high-performance organic–inorganic Z-scheme systems applied for artificial photosynthesis.

Results and Discussion

The COF-318/316-semiconductor (COF-318/316-SC) composites were synthesized by condensation of HHTP, TFPC/TFPN, and hydroxyl-containing oxide semiconductors (TiO_2, Bi_2WO_6, and α-Fe_2O_3; Scheme 1). The structures and successful preparation of COF-318 and COF-318-TiO_2-1/2/3/4 (20%, 25%, 40%, and 55% mass loading of TiO_2, respectively, abbreviated as COF-318-TiO_2 for 40 wt% content of TiO_2) were confirmed by powder X-ray diffraction (PXRD)

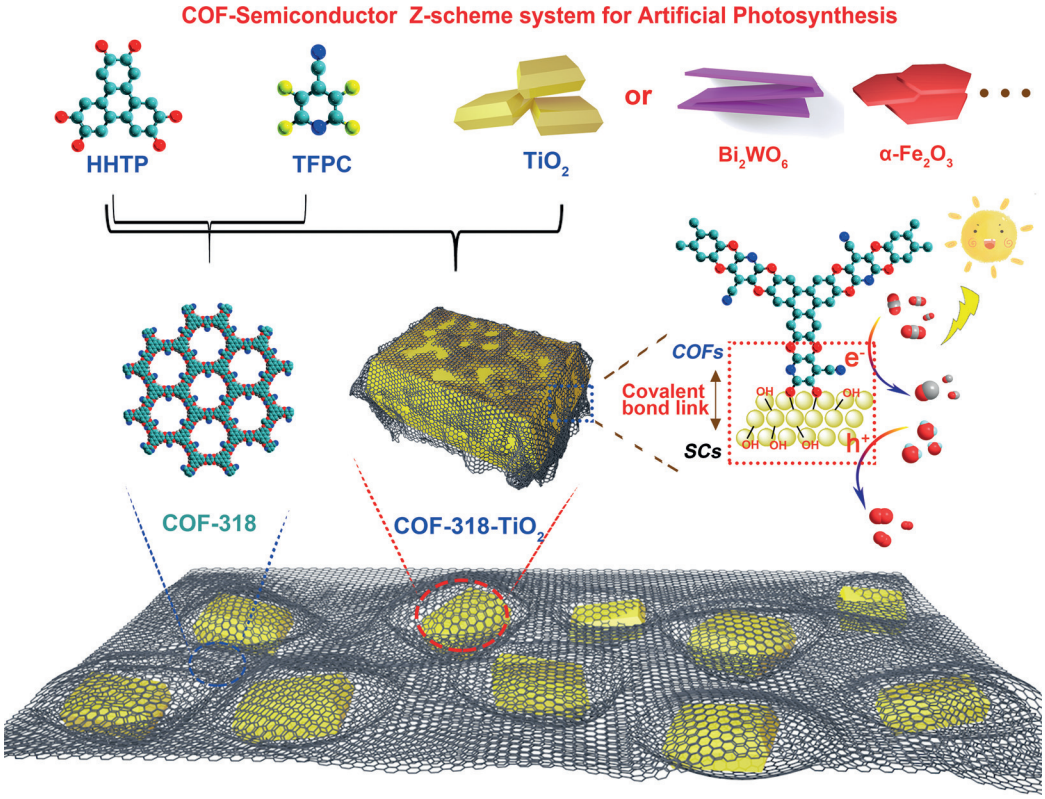

Scheme 1. Schematic representation of the preparation of COF-318-SCs via the condensation of COF-318 and semiconductor materials.

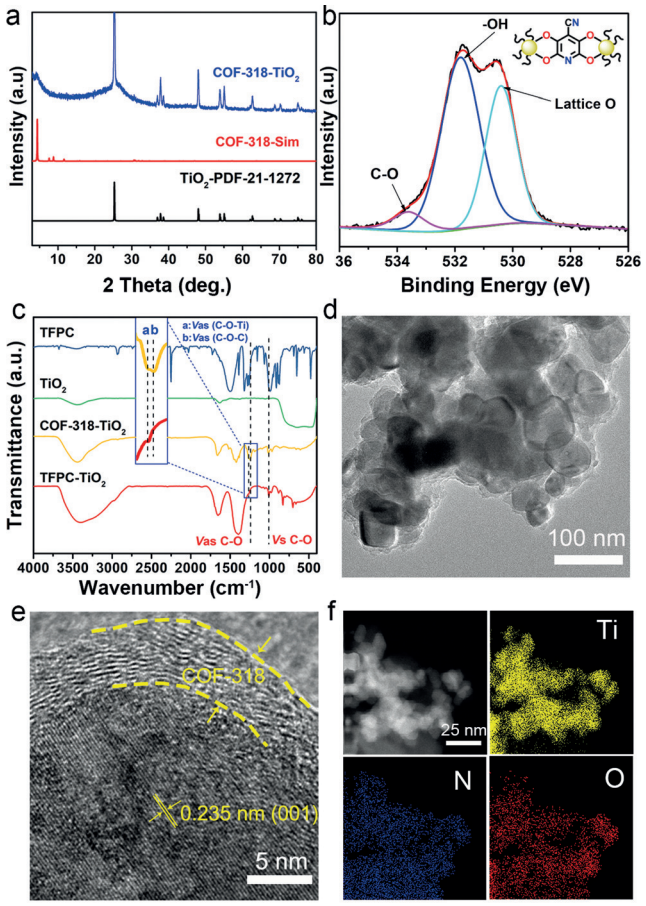

Figure 1. Characterization and morphology of COF-318-TiO_2. a) Experimental and simulated PXRD patterns of COF-318-TiO_2 (40 wt% for TiO_2); b) High-resolution O 1s XPS spectrum of model compound TFPC-TiO_2; c) FTIR spectrum of COF-318-TiO_2; d) TEM image of COF-318-TiO_2; e) HRTEM image and lattice fringes (the lattice fringe of 0.235 nm is attributed to the (001) face of TiO_2); f) High-angle annular-dark-field element mapping of COF-318-TiO_2.

patterns as shown in Figures 1a and S1,S2 (Supporting Information).

The presence of characteristic diffraction peaks at 4.38°, 7.53°, 8.82°, and 30.67° were attributed to the crystalline COF-318. The residual peaks in COF-318-TiO_2 agreed with the simulated PXRD patterns of anatase TiO_2 (PDF-21-1272). Proof of the covalent-bond connection was provided by X-ray photoelectron spectroscopy (XPS), Fourier-transform infrared (FTIR) spectroscopy, and DFT calculations. The XPS results showed that C–O bonds exist in the model compounds TFPC-TiO_2 and COF-318-TiO_2 (Figures 1b and S9–S15). In the FTIR spectrum (Figure 1c), the signal at 1012 cm^{-1} could be assigned to the symmetric stretching vibration of the dioxin C–O bond of COF-318-TiO_2, and it also existed in TFPC-TiO_2. The peak at 1243 cm^{-1} was assigned to the C–O–C asymmetric stretching vibration of COF-318 (b: Vas C–O–C in Figure 1c), while the signal at 1265 cm^{-1} was assigned to the C–O–Ti asymmetric stretching vibration (a: Vas C–O–Ti in Figure 1c). All these evidences illustrate that TiO_2 was successfully attached to COF-318/TFPC through C–O covalent bonds. The structure of the as-prepared COF-318-Bi_2WO_6 (40 wt% of Bi_2WO_6) and COF-318-α-Fe_2O_3 (40 wt% of α-Fe_2O_3) were also confirmed by PXRD (Figures S3,S4) and FTIR (Figures S7,S8). Similarly, the structures and successful preparation of COF-316 and COF-316-TiO_2 were confirmed by PXRD as shown in Figures S5,S6. The porous structures and surface areas of these samples were evaluated by N_2 sorption measurements at 77 K (Figures S16–S18). The surface area of COF-318-TiO_2 was calculated to be 196.386 $m^2 g^{-1}$ using the Brunauer–Emmett–Teller (BET) method, which is smaller than that of pure COF-318 (461.295 $m^2 g^{-1}$). The difference is due to the presence of TiO_2, which has a low surface area (26.484 $m^2 g^{-1}$). The pore size of COF-318 is distributing between ≈1.6 nm and ≈2.8 nm, which was calculated from the N_2 adsorption isotherms. This kind of pore also exists in COF-318-TiO_2 due to the introduced nonporosity of TiO_2. The TiO_2 mass content of COF-318-TiO_2 was calculated from thermogravimetric analysis (TGA; Figure S20).

The morphology of the COF-318-SCs was investigated by transmission electron microscopy (TEM) and scanning electron microscopy (SEM). Figures S21,S22 show SEM and TEM images of pure COF-318 and TiO_2. They reveal that the bulk COF-318 consists of graphene-like layered assemblies in thin nanosheets. The synthesized TiO_2 was in the anatase type with an average diameter of circa 50 nm. Significantly, from the TEM images of COF-318-TiO_2 (Figures 1d and S23), all TiO_2 was completely covered by COF-318, which indicates that there is a strong bonding interaction between TiO_2 and the COF. In the high-resolution TEM (HR-TEM) image (Figure 1e) of COF-318-TiO_2, the lattice fringe of 0.235 nm was attributed to the (001) face of TiO_2, while the outer covering with a thickness of 5–10 nm was attributed to the COF shell. Figure 1f shows the high-angle annular dark field (HAADF) image and energy-dispersive X-ray spectroscopy (EDX) elemental mapping of the COF-318-TiO_2 samples, signifying that the Ti, N, and O are evenly distributed within the COF-318-TiO_2 nanostructure. The morphologies and elemental mappings of COF-318-Bi_2WO_6 and COF-318-α-Fe_2O_3 are shown in Figures S24,S25. It can be clearly seen that Bi_2WO_6 and α-Fe_2O_3 are uniformly covered by COF-318 as well. The morphology of COF-316-TiO_2 was also investigated and is shown in Figure S26. These results indicate that the selected semiconductors are all encapsulated uniformly by the selected COFs, confirming the versatility of this approach.

Previous studies have confirmed that a high CO_2 adsorption capability is favorable to the improvement of the photocatalytic performance.[5b,14] CO_2 capacity measurements were performed for the synthesized hybrid materials COF-318-TiO_2 as well as pure COF and TiO_2 (Figures 2a and S19). The results show that COF-318-TiO_2 has high CO_2 uptakes of 27.5 and 19.0 $cm^3 g^{-1}$ at 273 K and 298 K, respectively. This large absorption ability is kinetically advantageous for CO_2 reduction.[15] After that, UV/Vis absorption measurements were performed, followed by a Tauc plot, to estimate the band gap for the as-prepared COF-318 and TiO_2 (Figure 2b) as well as Bi_2WO_6 and α-Fe_2O_3 (Figures S27,S28). Mott–Schottky (MS) measurements were conducted to determine the electronic band positions of the as-prepared materials (Figures 2c and S29–S32). The conduction-band position is −0.55

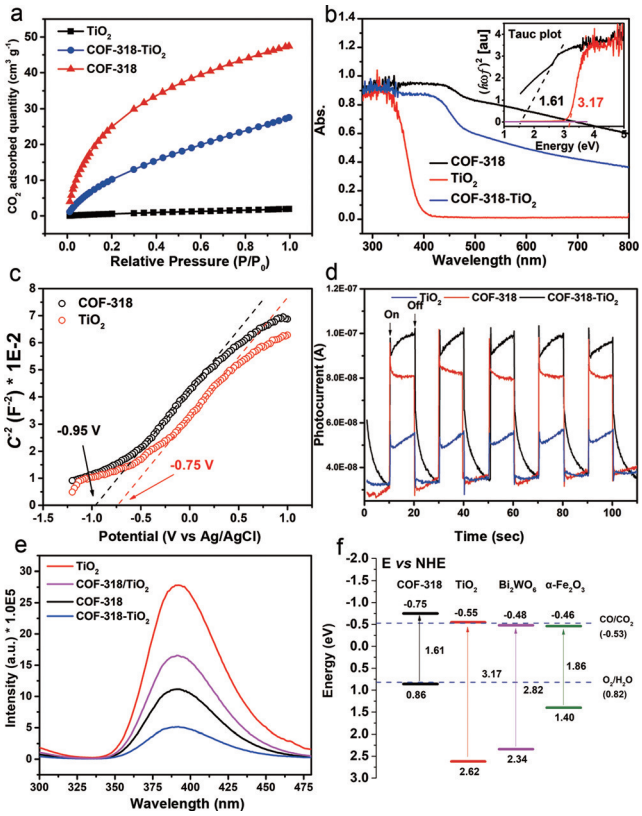

Figure 2. CO_2 absorption and optical properties of the COF-SCs. a) CO_2 adsorption curves of COF-318, TiO_2, and COF-318-TiO_2 measured at 273 K; b) Solid-state UV/Vis absorption spectra of COF-318, TiO_2, and COF-318-TiO_2 (Inset: Tauc plot). c) Mott–Schottky plot for COF-318 and TiO_2; d) Transient photocurrent response of COF-318-TiO_2, TiO_2, and COF-318-TiO_2; e) PL of COF-318, TiO_2, and COF-318-TiO_2; f) Band-structure diagram for COF-318, TiO_2, Bi_2WO_6, and α-Fe_2O_3.

and −0.75 eV (vs. NHE) for COF-318 and TiO_2. Combined with the band gap of COF-318 and TiO_2 from UV/Vis absorption data, the valence-band position of them can be determined as 0.86 and 2.62 eV, respectively.

The electron-transfer direction between COF-318 and TiO_2 and whether a Z-scheme or a type-II heterojunction was formed will be discussed in detail below. We based this on the idea that the existence of covalent-bond linking in the COF-318-TiO_2 heterojunction causes the superior photo-induced electron separation/transport efficiency compared to conventional heterojunctions. As a proof of concept, transient photocurrent response and photoluminescence (PL) measurements were conducted to investigate the charge-transfer behaviors (Figure 2d). As expected, the intensity of the transient photocurrent response of COF-318-TiO_2 turned out to be 3 times and 1.5 times higher than that of pure TiO_2 and COF-318, respectively. The transient-photocurrent-response intensities of COF-318-Bi_2WO_6 and COF-318-α-Fe_2O_3 were also much higher than those of COF-318, Bi_2WO_6, and α-Fe_2O_3, as shown in Figures S33,S34. The PL of COF-318-TiO_2 showed the weakest intensity of all (Figure 2e), much lower than that of the physical-mixture composite COF-318/TiO_2. All these results illustrate that the covalently linked heterojunction can effectively enhance electron–hole separation and prevent electron–hole recombination, which is attributed to an efficient electron transfer through the covalent bonds. At the same time, the electronic conductivity of the COF-SCs was also found to be better than that of the semiconductors in electrochemical impedance spectroscopy (EIS) measurements, as indicated by the radius of the preceding semicircle (Figures S35–S37), suggesting that the covalent linkage of COF and semiconductor can clearly enhance the charge transfer.

Theoretically, a photocatalyst needs a more negative conduction-band-minimum (CBM) potential than the theoretical CO_2 reduction potential to complete the CO_2RR. As for the H_2O oxidation reaction, a more positive valence-band-maximum (VBM) potential is needed to catalyze the H_2O/O_2 conversion.[6a] The optical band-structure diagrams of COF-318, TiO_2, Bi_2WO_6, and α-Fe_2O_3 are displayed in Figure 2f. The results show that COF-318 is capable of reducing CO_2 to many reductive carbon-based products (such as CO, CH_4, or HCOOH), and these semiconductors are capable of oxidizing H_2O to O_2. Based on this, the efficient bonding between COF-318 and semiconductors has great potential to complete the overall reaction (that is, CO_2RR with H_2O as the electron donor).

The photocatalytic CO_2-reduction performance was investigated with the gas–solid method under simulated sunlight irradiation ($\lambda = 380$–800 nm), without an additional photosensitizer, sacrificial agent, or co-catalyst. Detailed descriptions of the photocatalytic CO_2-reduction measurement are presented in the Supporting information (Section S3). Before the gas–solid photocatalytic reaction measurements, the COF-SCs were soak-washed with 60 °C *N*,*N*-dimethylformamide (DMF) and H_2O for 12 h, then transferred to a Soxhlet extractor and washed with tetrahydrofuran for 24 h. Finally, the product was evacuated at 150 °C under dynamic vacuum overnight to yield the activated sample. As shown in Figures 3a and S38, COF-318-TiO_2 displays an optimal CO formation rate of 278.7 μmol g^{-1}, much higher than 53.2 μmol g^{-1} for bulk COF-318 and 47.2 μmol g^{-1} for bulk TiO_2, revealing the advantage of the heterostructure. We also tested the performance of the other COF-SC heterojunctions COF-318-Bi_2WO_6 and COF-318-α-Fe_2O_3 (Figures 3b and S39). After forming a heterojunction with COF-318 and COF-316, in all cases the CO_2 reduction activity greatly improved compared to the bulk component. More importantly, the covalently connected COF-318-TiO_2 shows a much higher value than the physical mixture COF-318/TiO_2 (117.2 μmol g^{-1}, 40 wt% content of TiO_2), showing the superiority of the covalently linked heterojunction. This is, to our knowledge, one of the best performances reported for the overall CO_2 reduction with H_2O (see Table S1). The CO_2 reduction performance of the composites with different TiO_2 content shows a volcanic shape, and the performance is the highest at 40 wt% content, which is most likely due to the increased active-site exposure and more efficient electron transfer of the composites in an appropriate proportion.

During the photoreduction, this catalyst can simultaneously achieve the reaction of H_2O oxidation to O_2, which was

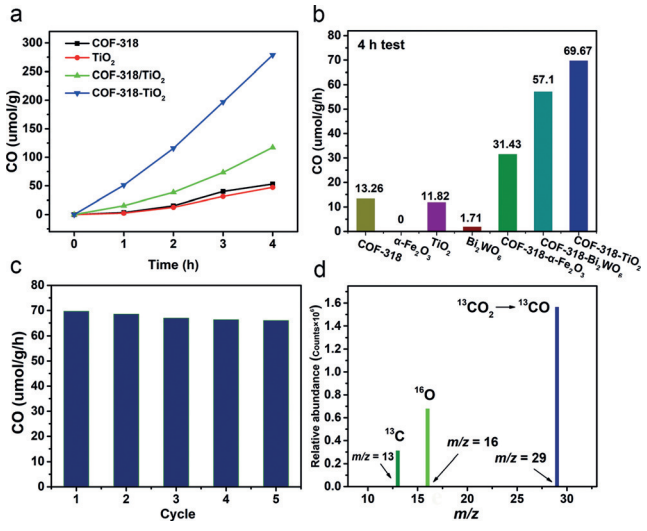

Figure 3. Photocatalytic CO_2RR performance of COF-SCs. a) Photocatalytic CO_2-to-CO performances of COF-318-TiO_2 for gas–solid CO_2 reduction compared with COF-318, TiO_2, and COF-318/TiO_2; b) Photocatalytic performances of various COF-318-SCs as well as bulk COF-318, TiO_2, Bi_2WO_6, and α-Fe_2O_3; c) Durability measurements of COF-318-TiO_2; d) Mass spectroscopy of ^{13}CO ($m/z = 29$) produced from the photocatalytic reduction of $^{13}CO_2$.

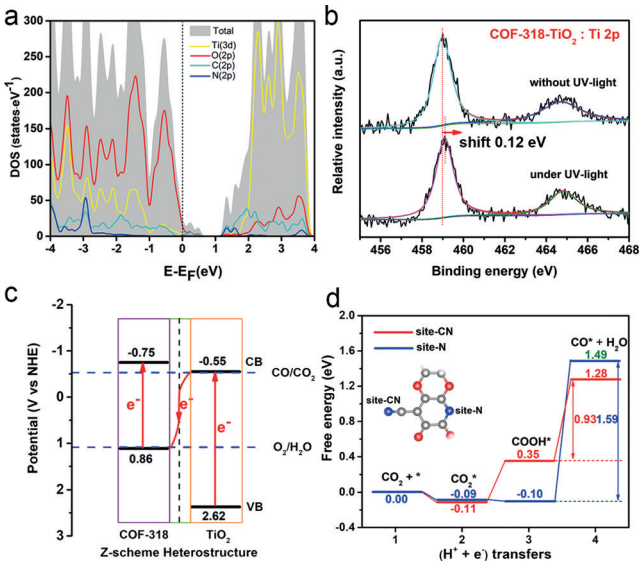

Figure 4. Mechanism and DFT calculations. a) Atom-projected density of states for COF-318(010)-TiO_2(001). b) High-resolution in-situ XPS for Ti 2p of COF-318-TiO_2 in the dark and under 365 nm LED irradiation; c) Schematic illustration of the charge-transfer process under light irradiation with the Z-scheme model; d) CO_2RR process on COF-318-TiO_2 based on DFT calculations.

confirmed by isotope-labeling experiments through mass spectrometry. The stability of the COF-318-TiO_2 hybrid was investigated by five consecutive runs with each run lasting 4 h under light irradiation. Here, the performances showed only negligible drops (Figure 3c). We then performed isotope-labeling experiments to ascertain the carbon and oxygen sources of the resulting products. As shown in the mass spectrum in Figure 3d, ^{13}CO ($m/z = 29$) was detected when using $^{13}CO_2$ as a substrate. Moreover, when H_2O was replaced by $H_2{}^{18}O$, $^{18}O_2$ ($m/z = 36$) and $^{18}O^{16}O$ ($m/z = 34$) were detected after the reaction (Figures S40,S41), affirming that the generated $^{18}O_2/O_2$ is derived from the oxidation of $H_2{}^{18}O/H_2O$. Crystallinity and structural integrity of the COF-318-SCs were retained after the reaction, as confirmed by PXRD (Figures S42–S44).

To investigate the connection mode between COF-318 and the semiconductor TiO_2, we investigated the adsorption of COF-318(010) on the TiO_2(001) and (101) facets from a theoretical point of view. Both adsorptions are thermodynamically favorable through the formation of a C_{COF}–O_{TiO2}–Ti_{5c} covalent connection ($d_{Ti5c-O} = 2.04$–2.10 Å), while the adsorption on TiO_2(001) is more stable than on (101), as shown in Figures S45,S46 (-0.80 vs. -0.72 eV). A more careful comparison of the density of states (DOS) for the individual components (TiO_2(001) and COF) and the COF-318(010)-TiO_2(001) composite shows interesting electronic characteristics (Figures 4a and S47). Through the connection, a new valence band (VB) and conduction band (CB) was formed by the insertion of C(2p) and N(2p) bands between the O(2p) and Ti(3d) bands of pure TiO_2(001), with a band gap of only 0.35 eV, indicating a photonic sensitization of the TiO_2 substrate by the COF layer. The Fermi level of COF-318(010)-TiO_2(001) moves inside the valence band by an increase of the energy of the O(2p) and Ti(3d) states. On the contrary, the lowest unoccupied Ti(3d) states are elevated to 1.5 eV due to the adsorption of COF-318. Consequently, a photoelectron would potentially transfer from TiO_2 to the COF-318 layer.

To clarify the electron-transfer direction between COF-318 and TiO_2 experimentally and whether it complies with the Z-scheme or type-II heterojunction pathway, high-resolution in-situ XPS measurements for the Ti 2p states of COF-318-TiO_2 were conducted (Figure 4b). The positive shift in the Ti 2p binding energy under UV irradiation is due to the electron-density decrease at the Ti sites.[16] These results show that the migration direction of the photogenerated electrons is from TiO_2 to COF-318, which is in line with the theoretical results. The proposed transfer path of the photogenerated electrons is shown in Figure 4c. In detail, by irradiation with UV/Vis light, both COF-318 and TiO_2 in COF-318-TiO_2 can be excited to generate electrons and holes, while the excited electrons of TiO_2 tend to transfer to COF-318 and, finally, accumulate at the pyridine/cyano moieties. Simultaneously, the remaining positive holes accumulate in the VB of TiO_2. The entire electron-transfer path forms a Z-scheme. Importantly, the Z-scheme of COF-318-TiO_2 takes advantage of the high photoreduction potential of COF-318 and the powerful photooxidation ability of TiO_2. Furthermore, the CO_2 reduction pathway was investigated via the computational hydrogen electrode model using DFT. Referring to the primitive steps for CO_2 reduction to CO, as presented in Figure 4d, the second proton-coupled electron-transfer step (*COOH → *CO) serves as the potential-determining step (PDS). To identify the specific active sites for CO_2 reduction in the COF, two possible reactive sites—N atoms in pyridine (site-N) and the cyano group (site-CN)—were considered for the reduc-

tion. The required free-energy change for the PDS is calculated to 1.59 and 0.93 eV for site-N and site-CN, respectively, suggesting a lower required overpotential for site-CN. Therefore, we propose that the cyano group could be a promising catalytic site for CO_2 photoreduction. From another point of view, the cyano group plays the role of an electron acceptor.[17] It should be noted that the ability to capture CO_2 is almost equivalent on both sites, while the CO_2 activation to *COOH is more favorable on site-N. This may lead to another possible pathway on pyridine N, lowering the difference between site-N and site-CN. Hence, the photogenerated electrons tend to aggregate at the cyano group, which is more conducive to the reduction of CO_2. As the second electron and proton inject into the −C≡N−*COOH unit, the *COOH finally turns into CO molecules and desorbs. The H_2O oxidation process in hole-doped TiO_2 has already been extensively studied and unanimously recognized. Overall, we can conclude that the pyridine group is beneficial to the first step of CO_2 activation to *COOH, and the cyano group is favorable for the second proton-coupled electron-transfer (*COO→*CO). Therefore, the presence of both pyridine and cyano groups lowers the overall energy barrier for the reduction of CO_2. As a result, compared with isolated cyano active sites in COF-316-TiO_2, the combination of pyridine and cyano groups causes a higher CO_2 reduction activity.

Conclusion

In summary, we developed a strategy to fabricate COFs coupled to inorganic oxide semiconductors through stable covalent bonds, forming organic–inorganic Z-scheme heterojunctions for artificial photosynthesis. Three types of semiconductors (TiO_2, Bi_2WO_6, and α-Fe_2O_3) and two types of COFs (COF-316 and COF-318) were selected to construct COF–semiconductor heterojunctions and used for photosynthetic gas–solid CO_2RR using H_2O as the electron donor, without additional photosensitizers, sacrificial agents, and cocatalysts. The covalently linked COF-318-TiO_2 Z-scheme heterojunction shows the highest CO production rate of 69.67 $\mu mol\,g^{-1}\,h^{-1}$, which is about six times higher than that of the pure COF-318 and TiO_2, and also much higher than that of the physical-mixture composites. Through comprehensive characterization and DFT calculations, we confirmed that the effective covalent coupling between organic framework and semiconductor enables photo-generated electrons to transfer efficiently between organic functional groups and the semiconductor. This feature results in the photoexcited electrons and holes accumulating in the COF and TiO_2, respectively, and can be efficiently used for CO_2 reduction and H_2O oxidation, thus simulated the artificial photosynthesis. Experiment and DFT calculations suggest the superiority of the coexistence of pyridine and cyano active sites in the COF photocatalyst for CO_2 reduction. This strategy represents a new insight for the future rational design of Z-scheme organic–inorganic heterojunctions for artificial photosynthesis.

Acknowledgements

This work was financially supported by NSFC (No. 21871141, 21871142, 21701085, and 21901122), the NSF of Jiangsu Province of China (No. BK20171032), the Natural Science Research of Jiangsu Higher Education Institutions of China (No. 17KJB150025 and 19KJB150011), and funded by the China Postdoctoral Science Foundation (No. 2018M630572 and 2019M651873), the Postgraduate Research & Practice Innovation Program of Jiangsu Province (KYCX19_0781), the Priority Academic Program Development of Jiangsu Higher Education Institutions, and the Foundation of Jiangsu Collaborative Innovation Center of Biomedical Functional Materials.

Conflict of interest

The authors declare no conflict of interest.

Keywords: artificial photosynthesis · CO_2 photoreduction · covalent organic frameworks · semiconductors · Z-scheme

How to cite: *Angew. Chem. Int. Ed.* **2020**, *59*, 6500–6506
Angew. Chem. **2020**, *132*, 6562–6568

[1] a) S. J. Davis, K. Caldeira, H. D. Matthews, *Science* **2010**, *329*, 1330–1333; b) T. M. Wigley, *Science* **2005**, *307*, 1766–1769; c) Y. Zeng, R. Zou, Y. Zhao, *Adv. Mater.* **2016**, *28*, 2855–2873.

[2] X. Liu, S. Inagaki, J. Gong, *Angew. Chem. Int. Ed.* **2016**, *55*, 14924–14950; *Angew. Chem.* **2016**, *128*, 15146–15174.

[3] a) S. Sato, T. Arai, T. Morikawa, K. Uemura, T. M. Suzuki, H. Tanaka, T. Kajino, *J. Am. Chem. Soc.* **2011**, *133*, 15240–15243; b) W. Tu, Y. Zhou, Z. Zou, *Adv. Mater.* **2014**, *26*, 4607–4626.

[4] a) L. Wang, W. Chen, D. Zhang, Y. Du, R. Amal, S. Qiao, J. Wu, Z. Yin, *Chem. Soc. Rev.* **2019**, *48*, 5310–5349; b) K. Maeda, *ACS Catal.* **2013**, *3*, 1486–1503; c) Y. Wang, Z. Zhang, L. Zhang, Z. Luo, J. Shen, H. Lin, J. Long, J. C. Wu, X. Fu, X. Wang, *J. Am. Chem. Soc.* **2018**, *140*, 14595–14598; d) K. Maeda, *Adv. Mater.* **2019**, *31*, 1808205; e) J. Ran, M. Jaroniec, S.-Z. Qiao, *Adv. Mater.* **2018**, *30*, 1704649.

[5] a) J. Bian, J. Feng, Z. Zhang, Z. Li, Y. Zhang, Y. Liu, S. Ali, Y. Qu, L. Bai, J. Xie, D. Tang, X. Li, F. Bai, J. Tang, L. Jing, *Angew. Chem. Int. Ed.* **2019**, *58*, 10873–10878; *Angew. Chem.* **2019**, *131*, 10989–10994; b) S. Wang, M. Xu, T. Peng, C. Zhang, T. Li, I. Hussain, J. Wang, B. Tan, *Nat. Commun.* **2019**, *10*, 676; c) J. Sun, J. Zhang, M. Zhang, M. Antonietti, X. Fu, X. Wang, *Nat. Commun.* **2012**, *3*, 1139.

[6] a) M. Lu, J. Liu, Q. Li, M. Zhang, M. Liu, J.-L. Wang, D.-Q. Yuan, Y.-Q. Lan, *Angew. Chem. Int. Ed.* **2019**, *58*, 12392–12397; *Angew. Chem.* **2019**, *131*, 12522–12527; b) Y.-Z. Zhang, B.-Q. Qia, J.-R. Ran, K. Davey, S.-Z. Qiao, *Adv. Energy Mater.* **2020**, https://doi.org/10.1002/aenm.201903879.

[7] a) Y. Song, Q. Sun, B. Aguila, S. Ma, *Adv. Sci.* **2019**, *6*, 1801410; b) Y. Zhang, J. Duan, D. Ma, P. Li, S. Li, H. Li, J. Zhou, X. Ma, X. Feng, B. Wang, *Angew. Chem. Int. Ed.* **2017**, *56*, 16313–16317; *Angew. Chem.* **2017**, *129*, 16531–16535; c) S. Yang, W. Hu, X. Zhang, P. He, B. Pattengale, C. Liu, M. Cendejas, I. Hermans, X. Zhang, J. Zhang, J. Huang, *J. Am. Chem. Soc.* **2018**, *140*, 14614–14618; d) W. Zhong, R. Sa, L. Li, Y. He, L. Li, J. Bi, Z. Zhuang, Y. Yu, Z. Zou, *J. Am. Chem. Soc.* **2019**, *141*, 7615–7621; e) Z. Fu, X. Wang, A. M. Gardner, X. Wang, S. Y. Chong, G. Neri, A. J.

Cowan, L. Liu, X. Li, A. Vogel, R. Clowes, M. Bilton, L. Chen, R. S. Sprick, A. I. Cooper, *Chem. Sci.* **2020**, *11*, 543 – 550; f) N. Huang, P. Wang, D. Jiang, *Nat. Rev. Mater.* **2016**, *1*, 16068.

[8] a) X. Wang, L. Chen, S. Y. Chong, M. A. Little, Y. Wu, W. H. Zhu, R. Clowes, Y. Yan, M. A. Zwijnenburg, R. S. Sprick, A. I. Cooper, *Nat. Chem.* **2018**, *10*, 1180 – 1189; b) S. Wan, F. Gándara, A. Asano, H. Furukawa, A. Saeki, S. K. Dey, L. Liao, M. W. Ambrogio, Y. Y. Botros, X. Duan, S. Seki, J. F. Stoddart, O. M. Yaghi, *Chem. Mater.* **2011**, *23*, 4094 – 4097.

[9] a) T. Arai, S. Sato, T. Kajino, T. Morikawa, *Energy Environ. Sci.* **2013**, *6*, 1274 – 1282; b) T. Hisatomi, J. Kubota, K. Domen, *Chem. Soc. Rev.* **2014**, *43*, 7520 – 7535.

[10] a) L. Grill, M. Dyer, L. Lafferentz, M. Persson, M. V. Peters, S. Hecht, *Nat. Nanotechnol.* **2007**, *2*, 687; b) R. E. Holmlin, R. F. Ismagilov, R. Haag, V. Mujica, M. A. Ratner, M. A. Rampi, G. M. Whitesides, *Angew. Chem. Int. Ed.* **2001**, *40*, 2316 – 2320; *Angew. Chem.* **2001**, *113*, 2378 – 2382; c) X. Guo, J. P. Small, J. E. Klare, Y. Wang, M. S. Purewal, I. W. Tam, B. H. Hong, R. Caldwell, L. Huang, S. Brien, J. Yan, R. Breslow, S. J. Wind, J. Hone, P. Kim, C. Nuckolls, *Science* **2006**, *311*, 356; d) C. Jia, A. Migliore, N. Xin, S. Huang, J. Wang, Q. Yang, S. Wang, H. Chen, D. Wang, B. Feng, Z. Liu, G. Zhang, D.-H. Qu, H. Tian, M. A. Ratner, H. Q. Xu, A. Nitzan, X. Guo, *Science* **2016**, *352*, 1443; e) M. Yamamoto, L. Wang, F. Li, T. Fukushima, K. Tanaka, L. Sun, H. Imahori, *Chem. Sci.* **2016**, *7*, 1430 – 1439.

[11] X. Guan, H. Li, Y. Ma, M. Xue, Q. Fang, Y. Yan, V. Valtchev, S. Qiu, *Nat. Chem.* **2019**, *11*, 587 – 594.

[12] B. Zhang, M. Wei, H. Mao, X. Pei, S. A. Alshmimri, J. A. Reimer, O. M. Yaghi, *J. Am. Chem. Soc.* **2018**, *140*, 12715 – 12719.

[13] a) E. McCafferty, J. P. Wightman, *Surf. Interface Anal.* **1998**, *26*, 549 – 564; b) S. P. Pujari, L. Scheres, A. T. M. Marcelis, H. Zuilhof, *Angew. Chem. Int. Ed.* **2014**, *53*, 6322 – 6356; *Angew. Chem.* **2014**, *126*, 6438 – 6474.

[14] a) D. Wang, R. Huang, W. Liu, D. Sun, Z. Li, *ACS Catal.* **2014**, *4*, 4254 – 4260; b) R. Li, W. Zhang, K. Zhou, *Adv. Mater.* **2018**, *30*, 1705512; c) M. Lu, Q. Li, J. Liu, F.-M. Zhang, L. Zhang, J.-L. Wang, Z.-H. Kang, Y.-Q. Lan, *Appl. Catal. B* **2019**, *254*, 624 – 633.

[15] a) H. Zhang, J. Wei, J. Dong, G. Liu, L. Shi, P. An, G. Zhao, J. Kong, X. Wang, X. Meng, J. Zhang, J. Ye, *Angew. Chem. Int. Ed.* **2016**, *55*, 14310 – 14314; *Angew. Chem.* **2016**, *128*, 14522 – 14526; b) S. Guo, H. Zhang, Y. Chen, Z. Liu, B. Yu, Y. Zhao, Z. Yang, B. Han, Z. Liu, *ACS Catal.* **2018**, *8*, 4576 – 4581.

[16] J. Low, B. Dai, T. Tong, C. Jiang, J. Yu, *Adv. Mater.* **2019**, *31*, 1802981.

[17] a) G. Liu, G. Zhao, W. Zhou, Y. Liu, H. Pang, H. Zhang, D. Hao, X. Meng, P. Li, T. Kako, J. Ye, *Adv. Funct. Mater.* **2016**, *26*, 6822 – 6829; b) V. W.-h. Lau, I. Moudrakovski, T. Botari, S. Weinberger, M. B. Mesch, V. Duppel, J. Senker, V. Blum, B. V. Lotsch, *Nat. Commun.* **2016**, *7*, 12165.

Manuscript received: January 18, 2020
Revised manuscript received: January 26, 2020
Accepted manuscript online: January 27, 2020
Version of record online: February 25, 2020

